Anomalous indirect carrier relaxation in direct band gap atomically thin gallium telluride

Manobina Karmakar [ORCID]

Department of Physics, Indian Institute of Technology Kharagpur, Kharagpur 721302, India
and NanoScience Technology Center, University of Central Florida, Orlando, Florida 32826, USA

Partha Kumbhakar[*]

Metallurgical and Materials Engineering, Indian Institute of Technology Kharagpur, Kharagpur 721302, India

Tara Singha [ORCID]

Department of Physics, Indian Institute of Technology Kharagpur, Kharagpur 721302, India

Chandra Sekhar Tiwary[†]

Metallurgical and Materials Engineering, Indian Institute of Technology Kharagpur, Kharagpur 721302, India

Debashis Chanda[‡]

NanoScience Technology Center, University of Central Florida, Orlando, Florida 32826, USA;
Department of Physics, University of Central Florida, Orlando, Florida 32826, USA;
and CREOL, The College of Optics and Photonics, University of Central Florida, Orlando, Florida 32826, USA

Prasanta Kumar Datta [ORCID][§]

Department of Physics, Indian Institute of Technology Kharagpur, Kharagpur 721302, India

We report ultrafast studies on atomically thin Gallium telluride, a 2D metal monochalcogenide that has appeared to display superior photodetection properties in visible frequencies. Pump photon energy-dependent spectroscopic studies reveal that photoinduced carriers in this direct band-gap material undergo indirect relaxation within ∼30 ps of photoexcitation, which is at least an order slower than that of most 2D materials. Despite the direct band-gap nature, slow and indirect carrier relaxation places this layered material as a prime candidate in the multitude of atomically thin semiconductor-based photodetectors and highlights the potential for prospective optoelectronic applications.

I. INTRODUCTION

Due to the two-dimensional carrier confinement and high mobility, multiple two-dimensional materials have been explored as prospective candidates for next-generation low-cost, highly efficient, and low size, weight, and power photodetectors [1]. The photodetection efficacy of a material is gauged over the high photoresponsivity and fast response time of the device.

In the continuous quest of optimizing the figure of merit, i.e., sensitivity (D*) atomically thin III-VI metal monochalcogenides (MMCs) of type MX (M = Ga, In, X = S, Se, Te) have recently appeared as the front-runners displaying D* of $\sim 10^9 - 10^{11}$ HzAW^{-1} [2–4]. Gallium telluride (GaTe)-

based photodetectors exhibit high photoresponsivity $\sim 10^3 - 10^6$ AW^{-1} [2,5,6], which is orders of magnitude higher than that of most of the transition metal dichalcogenides and other 2D materials [6–12]. A physical explanation of this extraordinary photodetection sensitivity remained unexplained and calls for an in-depth understanding of the fundamental carrier dynamics of this material.

It is widely known that strong photoabsorption oscillator strength and slow photogenerated carrier relaxation are the main driving forces behind high photosensitivity in bulk or low-dimensional materials. However, these are two mutually exclusive requirements. A direct gap semiconductor offers strong optical absorption, but fast (direct) carrier relaxation and hence poor carrier collection probability. On the other hand, an indirect gap material exhibit slow carrier relaxation, but low absorption strength. Carrier relaxation timescale is a crucial parameter to strike a balance for efficient carrier collection and higher sensitivity (D*).

Here, we present the photoinduced carrier dynamics in 2D GaTe for the first time through femtosecond transient absorption spectroscopy and elucidate, yet to be understood,

---

[*]Present address: Department of Physics and Electronics, CHRIST (Deemed to be University), Bangalore 560029, India.
[†]chandra.tiwary@metal.iitkgp.ac.in
[‡]debashis.chanda@ucf.edu
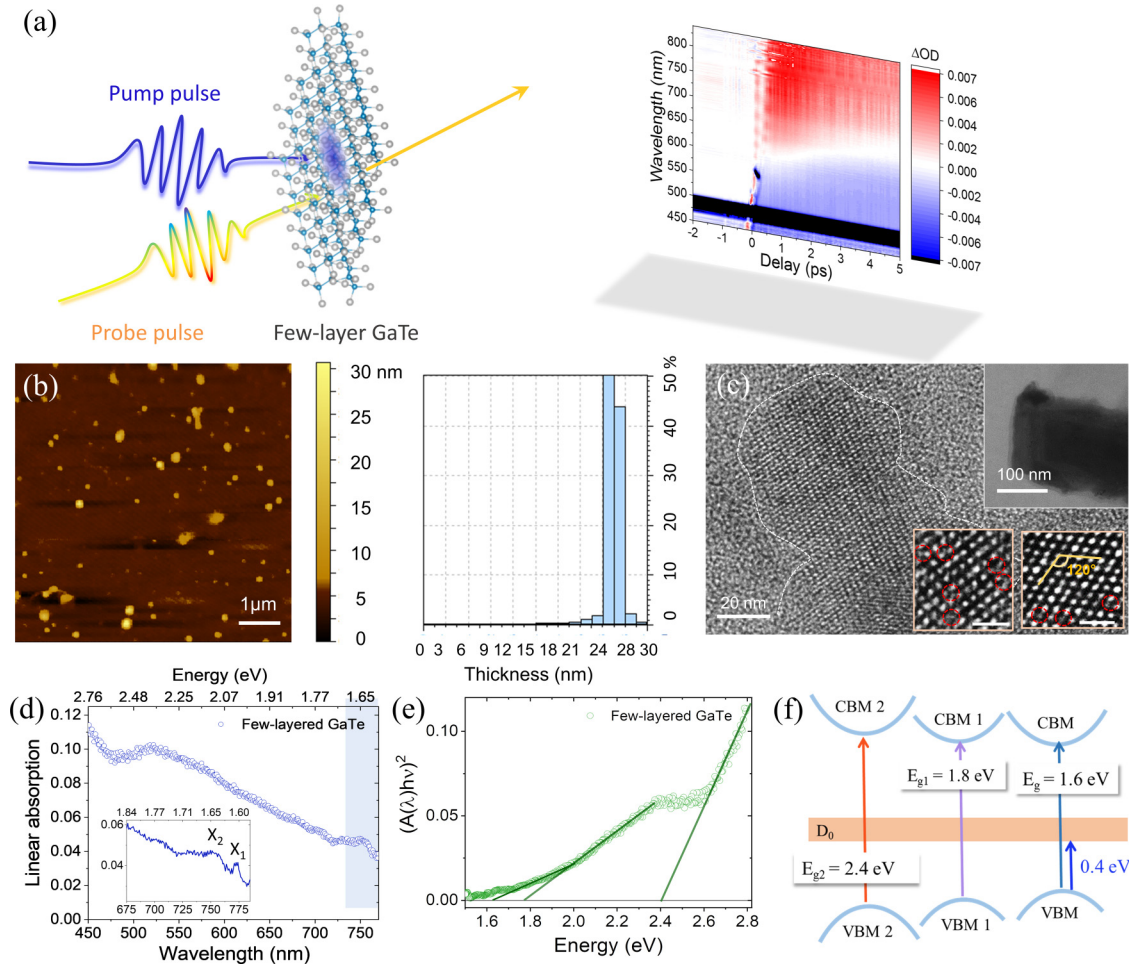[§]pkdatta@phy.iitkgp.ac.in

FIG. 1. (a) A schematic illustration of transient absorption spectroscopy of layered GaTe. (b) Atomic force microscopic image of 2D few-layered GaTe and corresponding histogram plot of the flake heights depict an average 25 nm sample thickness of our 2D GaTe flakes. (c) High-resolution transmission electron microscopic image of 2D GaTe. The upper right inset is a low-resolution image of a large and thin flake. The two lower right insets display the crystalline structure of GaTe. Here the scale bar corresponds to 1 nm. Red circles identify defects or vacancies. (d) The linear absorption spectrum of a few-layered GaTe in the visible region. The inset display a magnified spectrum in the wavelength range of 675 nm to 815 nm. Two excitonic absorption peaks (X_1 and X_2) are observed in this region. (e) Tauc's plot for a direct band gap of a few-layered GaTe identifies three direct bands around 1.6 eV, 1.8 eV, and 2,4 eV. (f) Schematic band structure of GaTe that depicts three direct bands at separate quasimomenta and midgap defect levels.

efficient light-to-electricity conversion pathways. Broad tuning of pump photon energy in the transient experiments reveals that despite the direct nature of the band gap in 2D GaTe, the photoinduced free carriers relax via indirect recombination, which happens to be about an order slower than the typical direct recombination timescales. Hence, unlike other 2D materials, GaTe presents a unique combination of the two features required for efficient photodetection, i.e., direct band gap and indirect carrier relaxation. Following the above band-gap photoabsorption, while hot carriers cool down to populate the band edge, a mismatch in the electron and hole momentum results from unequal effective masses of electrons and holes (heavy electrons, light holes). Therefore, unlike most direct band-gap materials, different carrier cooling times in valance and conduction bands eventually forbid fast, direct electron-hole recombination. Moreover, we found that elevated midgap defect states do not influence the free carrier relaxation rates. Slow and defect-tolerant carrier relaxation distinguishes GaTe from other 2D materials and explains the

reason behind exceptionally high photoresponsivity. Our paper reveals the unique carrier dynamics of this class of direct band gap indirect carrier relaxation 2D materials. It sheds light on the prospects of the efficient optoelectronic applications of this unique material.

II. RESULTS AND DISCUSSION

We have prepared layered GaTe flakes through a solvent-based liquid-phase exfoliation [13] (see Ref. [14], Sec. S1). As this paper aims to explore the application prospects of the material, a scalable method of preparation [15] has been chosen instead of mechanical exfoliation and chemical vapor deposition (CVD) that lacks the essential scalability for mass device fabrication. Figure 1(b) displays an atomic force microscopic image of the prepared few-layered GaTe. The statistical height distribution reveals an average flake thickness of 25 nm [right panel of Fig. 1(b)]. High-resolution transmission electron microscopy images of the prepared 2D flakes are

shown in Fig. 1(c). The upper right inset shows a large flake having a lateral dimension around hundreds of nm. Several point defects are distinguishable from the high-resolution images in the lower right insets. We estimate a defect density $\sim 10^{14}$ per cm^2 (about one order higher than earlier reports in exfoliated and CVD-grown few-layered transition metal dichalcogenides (TMDC) materials [16]).

All the optical measurements on layered GaTe dispersed in a solvent (N, N-dimethylformamide) are performed within 10 h of sample preparation unless otherwise mentioned and are repeatable. Additional discussion on sample stability can be found in Sec. S4 of Ref. [14].

A. Steady-state absorption properties

The steady-state, linear absorption spectrum of few-layered gallium telluride is obtained using a low-intensity, broadband supercontinuum pulse, generated through focusing 800 nm, 50 fs pulse in a CaF$_2$ crystal [Fig. 1(d)]. A broadband absorption in the wavelength range of 450 nm to 780 nm is observed. Two weak absorption peaks are identified around 751 nm ($E_{X_2}^{2D} = 1.65$ eV) and 773 nm ($E_{X_1}^{2D} = 1.60$ eV). We attribute these features to X_2 and X_1 excitons, respectively. The weak excitonic effects, as indicated by the low absorption oscillator strengths, originate from the low binding energies (< 20 meV) [17,18]. To identify the direct band-gap [19] transitions, we present Tauc's plot in Fig. 1(e). Few-layered GaTe possesses a direct band gap around $E_g^{2D} = 1.6$ eV. This is consistent with previous reports [20–22]. We denote this as the fundamental band gap (FBG). In addition, two direct band gaps, $E_{g1}^{2D} = 1.8$ eV and $E_{g2}^{2D} = 2.4$ eV are observed. The observation of two more higher-energetic direct band gaps is consistent with the theoretically predicted multivalley nature of GaTe. The absorption features in the visible region do not follow exponential variation with photon energy ruling out possibilities of Urbach tails in the visible frequencies [23].

As observed in the TEM images, some defects are prevalent in the atomically thin layers of GaTe. Further investigation of absorption properties in the near-IR domain reveals weak midgap absorption. Further details on the sub-band-gap states are provided in Sec. S1 of Ref. [14]. Figure 1(f) displays a schematic band structure of few-layered GaTe, as we comprehend from the linear absorption spectrum. Valance band global maxima (conduction band global minima) corresponding to FBG is denoted by VBM (CBM). We identify other valance (VBM 1,2) and conduction band extrema (CBM 1,2) at different quasimomenta corresponding to E_{g1}^{2D} and E_{g2}^{2D} band gaps. Theoretically calculated band structure [19] of GaTe predicts the direct band gap of 1.65 eV at Z point (FBG) and slightly higher band gaps at P and M points. Therefore, observed E_{g1}^{2D} may originate from direct transitions at P and/or M point (see S1 of Ref. [19]). A subsequent higher-energetic direct band, with band gap ~ 3 eV, is observed around the U' point. We attribute this band to E_{g2}^{2D}. Note we often drop the superscript 2D for convenience while denoting band gaps.

B. Photoinduced carrier dynamics

To understand the photoinduced carrier dynamics thoroughly, we perform transient absorption spectroscopy with various pump excitation conditions. The sensitivity of our setup is well-tested [24–27]. We tune the pump wavelength from 400 nm (3.1 eV) to 800 nm (1.55 eV) and probe the ultrafast changes in the optical spectrum. In this paper, we use pump excitation fluence of order 10 μJ/cm^2. The excitation density of the broadband supercontinuum probe is (at least orders weaker) weak and does not excite the system and only measures the change in the transition probabilities of the material following pump excitation [28]. We measure the differential absorption (ΔOD), given by

$$\Delta OD(\lambda, t) = A_{\text{probe}}^{\text{pump}}(\lambda, t) - A_{\text{probe}}(\lambda), \tag{1}$$

where $A_{\text{probe}}^{\text{pump}}$ and A_{probe} signifies probe absorption in the presence and absence of pump excitation, respectively.

First, we photoexcite layered GaTe with a 485 nm (= 2.55 eV) pump that possesses photon energy greater than the three direct bands and ensures photoinduced carrier population (both electrons in the conduction band and holes in the valance band) in all three bands (band gaps E_g, E_{g1}^{2D}, and E_{g2}^{2D}). Figure 2(a) plots the color map of ΔOD as a function of probe delay and probe wavelength in the visible region. Differential absorption spectrum at a few chosen delays in Fig. 3(a) of Ref. [14] further portrays the temporal evolution of the ΔOD spectrum. We observe a broadband negative ΔOD feature at lower wavelengths that extends up to $\sim 560 - 620$ nm, and a positive absorption is observed at the higher wavelengths.

As the differential absorption spectra exhibit negative and positive absorption features through a continuous and broad range of wavelengths, the transient dynamics in the visible frequencies are predominantly dictated by unbound charge carriers and not excitons. Energetic positions of the negative ΔOD regions coinciding the direct band gaps E_g^{2D}, E_{g1}^{2D}, and E_{g2}^{2D} indicates state filling (also known as ground state bleaching) of these band gaps through the pump-induced carriers. Existence of probe-induced nonlinear phenomena, like stimulated emission, are discarded through repeated transient measurements with varying probe intensities. We do not observe any difference in the differential absorption spectrum while changing the probe intensity by an order. Therefore, we rule out (probe-induced) stimulated emission as the origin of negative ΔOD, which further confirms the aforesaid state-filling effect in the direct bands.

On the other hand, the positive ΔOD feature usually originates from photoinduced absorption due to excited state absorption (ESA). Pump excitation populates an intermediate state and the probe enables a further transition from this state to the deeper levels of the conduction band. Therefore, the temporal evolution of the ESA identifies the dynamics of the intermediate state. To investigate the energetic distribution of the ESA, we also perform transient absorption measurements in the near-infrared region up to 1.35 μm and observe a featureless positive ΔOD [see Fig. 2(b)] response corresponding to ESA. As evident from the contour plots in Figs. 2(a) and 2(b), the temporal evolution of ΔOD from 600 nm to 1300 nm is dominated by ESA that follows similar dynamics throughout the broad spectral range. Figure 2(e) provides more demonstration; similar dynamics at 750 nm and 1275 nm probes are discernible from the plot. The next section elaborates on the carrier dynamics that eventually help
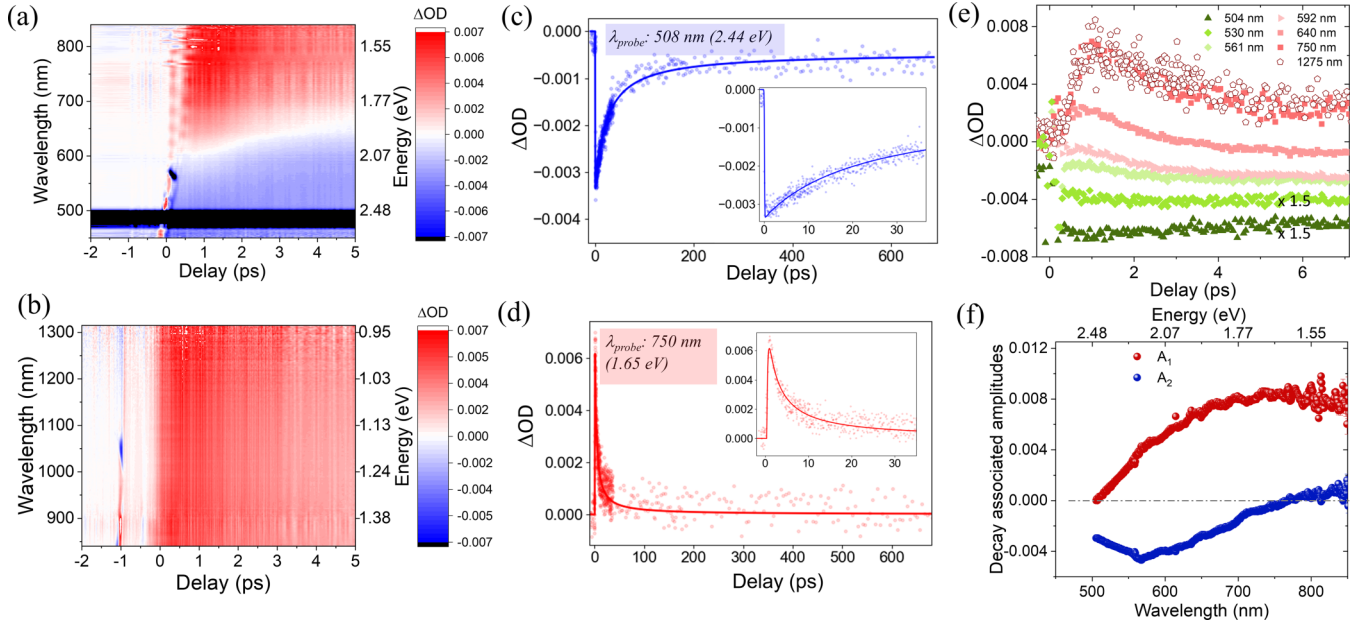
FIG. 2. (a) ΔOD spectral map at (a) visible (b) near infrared probe wavelengths corresponding to 485 nm pump excitation (fluence: $22\,\mu J/cm^2$) for probe delays -2 ps to 5 ps. Temporal evolution of ΔOD corresponding to (c) 508 nm and (d) 750 nm probe wavelengths. Insets plot the ΔOD versus delay at the initial probe delays (up to 35 ps). (e) ΔOD variation with delay for various probe wavelengths ranging from 504 nm to 1275 nm. (f) Decay-associated amplitudes corresponding to state-filling (A_2) and excited-state absorption (A_1) as obtained from global analysis of the transient absorption spectrum in the visible region.

to throw more light on the intermediate level, which enables the broadband ESA effect.

The following discussion on photoinduced carrier dynamics is divided into three subsections, particularly elaborating on (1) overall carrier relaxation rates, (2) the nature of electron-hole recombination: direct or indirect, and (3) the role of defect states in carrier dynamics in GaTe.

1. Carrier relaxation

The temporal evolution of differential absorption corresponding to the negative and positive ΔOD feature, particularly at 508 nm and 750 nm is presented in Figs. 2(c) and 2(d). Typically, in layered semiconductors, free carriers recombine nonradiatively through defect-assisted recombination and electron-hole recombination, which follow first-order (mono-molecular) and second-order (bimolecular) decay kinetics, respectively [29]. The electron-hole recombination, whether direct or indirect (e.g., phonon-assisted), follows second-order recombination. To identify the order of the relaxation processes, ΔOD^{-1} versus delay variation is followed [30]. Figure 5 in Ref. [14] plots the same at 515 nm and 750 nm probe wavelengths. ΔOD^{-1} follow linear variation with probe delay in both cases. This indicates second-order electron-hole recombination dominates the carrier dynamics [30]. To probe the specific rate constants, ΔOD dynamics corresponding to state filling and ESA are modeled as follows:

$$\Delta OD(\lambda, t) = \frac{A_1(1 - e^{-k_1^r t})}{1 - k_2' N_0' t}; \lambda = 750 \text{ nm} \quad (2a)$$

$$= \left(\frac{A_2}{1 - k_2 N_0 t} + A_2' \Theta(0) \right) * \text{IRF}; \lambda = 508 \text{ nm}, \quad (2b)$$

where A_1, A_2, and A_2' are amplitude constants and N_0 and N_0' are the photoexcited carrier densities participating in state filling and ESA. k_1^r incorporates the rise-time constant for the slow rise of the ΔOD response in the ESA region. k_2 and k_2' are second-order electron-hole recombination constants that dictate the decay of state filling and ESA, respectively. The nonvarying offset in ΔOD values at longer delays, specifically in the lower wavelength region corresponding to state-filling effect [see Fig. 2(c)], suggests a contribution of slower decay process (few ns or longer). To incorporate this in the numerical fitting, we include a step function [$\Theta(0)$], as this effect is practically constant in the timescales that we are interested in. Note that the rising part of ESA is considered through $(1 - e^{-k_1^r t})$ term in the numerator, yet the rise time of the state-filling effect is assumed to be IRF (instrument response function) limited. This assumption simplifies the problem without affecting the decay parameters for the following two reasons: (1) The rise part of the $|\Delta OD|$ in the state-filling region is dominated by coherent artifacts due to possible cross-phase modulation [31,32] and displays nontrivial oscillations instead of a monotonic rise (see Sec. S2.3 of Ref. [14] for a general discussion on coherent artifacts). However, these coherent effects are not applicable to relaxation dynamics. (2) ΔOD reverts at much slower dynamics compared to its fast (yet not instantaneous) appearance. Hence, the assumption in the rising part of the ΔOD does not affect the decay parameters for carrier relaxation. The solid lines in Figs. 2(c) and 2(d) represent the fitted curves that follow the scattered plots corresponding to the experimental data. Fitted parameters are mentioned in Tables I and II.

Interestingly, $k_2 N_0$ and $k_2' N_0'$, i.e., the product of second-order recombination rate constant and injected carrier density corresponding to state filling and ESA differ by one order.

TABLE I. Fitted parameters corresponding to excited state absorption.

λ (nm)	k_1^r (ps^{-1})	$k_2'N_0'$ (ps^{-1})	A_1
750	4.4 ± 0.7	-0.44 ± 0.03	0.008 ± 0.004

This observation suggests that $k_2' > k_2$, that is, the recombination rate constant of the electronic levels associated with ESA is higher than that of state filling. This observation indicates that the electronic level participating in the state-filling effect is not acting as the intermediate state for the ESA. Hence, it is evident that conduction band levels corresponding to E_g^{2D}, E_{g1}^{2D}, and E_{g2}^{2D} band gaps do not contribute as the intermediate state for ESA. Therefore, the midgap defect levels are attributed to these intermediate states.

As observed in Figs. 2(a) and 2(b), GaTe displays a sign reversal of ΔOD as one moves from lower to higher wavelengths. To highlight the initial dynamics in the state filling, ESA, and the intermediate spectral region, ΔOD up to 7 ps is depicted for different probe wavelengths ranging from 504 nm to 1275 nm in Fig. 2(e). In the case of the intermediate wavelengths (561 nm, 592 nm, 640 nm), the initial ΔOD dynamics displays a superposition of slower state-filling dynamics and faster ESA dynamics. To confirm this, a global analysis is performed that identifies the spectral attributes of the ESA and state-filling effect and, specifically, their spectral overlap (see Sec. S3, Ref. [14]). The relative spectral contribution of the two effects is clearly identified and is presented in Fig. 2(f). The onset of the state-filling effect is around 750 nm, i.e., ∼1.65 eV, nearly the same as the predicted band gap E_g^{2D}. State-filling effect of the higher energetic bands (E_{g1}^{2D}, E_{g2}^{2D}) are present in the lower wavelength regions.

2. Electron-hole recombination: Direct or indirect?

Few-layered GaTe is a direct band-gap material. The Tauc analysis of the linear absorption spectrum also suggests the same. From the photoinduced state-filling dynamics, we confirmed that the photo-induced carriers undergo second-order recombination.

State filling of any absorption band stems from either one or both of the following: population of the valance band through photoexcited holes and the population of the conduction band through photo-excited electrons [25,33]. Hence, the roles of both types of charge carriers are not guaranteed in the transient dynamics. Hence, the observed second-order recombination may arise from direct or indirect electron-hole recombination (i.e., electrons and holes reside in conduction and valance band of different valleys before recombination). In case the recombination process is direct, the second-order carrier relaxation can only be observed while the material is excited with pump photon energies at least equivalent to the

TABLE II. Fitted parameters corresponding to state filling.

λ (nm)	k_2N_0 (ps^{-1})	A_2	A_2'
508	-0.043 ± 0.003	-0.0029 ± 0.0005	-0.00046 ± 0.00004

absorption band. To have an insight into the nature of the recombination process, the pump photon energy is tuned in a broad range (400 nm to 750 nm ≡ 1.65 eV to 3.1 eV) and the state-filling dynamics, especially in the band E_{g2}^{2D} is investigated. Figure 3(a) presents the ΔOD spectra at 1 ps delay followed by different pump excitation, λ_p: 400 (fluence: 32 μJ/cm^2), 485, 650, 700 (fluence: 22 μJ/m^2), and 750 nm (fluence: 24 μJ/cm^2). ΔOD spectra appear to have very similar state fillings and ESA features irrespective of the pump wavelength. In each case, the state-filling effect is maximum in the wavelength range of 500 nm to 600 nm (also see Fig. 5, Ref. [14]). Notably, we did not observe any transient response of GaTe following 800 nm (1.55 eV) excitation, which is below the FBG. The state-filling and ESA features in the differential absorption spectra appear irrespective of the pump photon energy, provided the pump photon energy is above the FBG. It is quite intriguing that state filing in E_{g2}^{2D} appears even when the pump photon has less energy than the corresponding band. As we observe similar ΔOD amplitudes for above and below band (E_{g2}^{2D}) excitation with similar fluence, we exclude nonlinear, multiphoton absorption to be involved in the observed transient response corresponding to the lower energy photons. The appearance of the state-filling effect in the absorption band(s) following the below band-gap excitation can be explained by the pump-induced population of holes in the valance band; however, energy conservation precludes electrons from populating the corresponding conduction band level through the vertical transition. All the below-band-gap pump photon energies utilized in this experiment enable electronic transition at least in FBG, i.e., E_g^{2D} (from global valance band maxima to global conduction band minima). Photoexcited holes in the different valleys in valance bands VBM, VBM 1, and VBM 2 [see Fig. 1(f)] corresponding to the direct bands (E_g, E_{g1}, E_{g2}) introduce state filling. Similarly, the population of defect levels at all λ_{pump} enables ESA in the deeper conduction band levels.

We investigate the effect of pump photon energy on the initial build-up of the state-filling effect. ΔOD dynamics corresponding to different pump excitations at 508 nm probe up to 7 ps probe delay are observed in Fig. 3(c). It is interesting to note that in the presence of 400 nm and 485 nm pump excitation, ΔOD builds up with approximated time constants, $\tau_r = 0.7 \pm 0.2$ ps and $\tau_r = 0.5 \pm 0.2$ ps (obtained by fitting a single exponential function to ΔOD from 0 ps to 2 ps, neglecting the coherent artifacts). On the contrary, ΔOD peaks instantaneously (the underlying mechanism is faster than the instrumental response function of 150 fs) with respect to the temporal overlap of the pump and probe pulse while the pump wavelengths are tuned to 650 nm and 750 nm. Both 400 nm and 485 nm excitation is blue-detuned to E_{g2}^{2D} by 0.66 eV and 0.12 eV, respectively, and, hence, excites hot electrons in the FBG (E_{g2}^{2D}). Therefore, the rise-time components τ_r are attributed to carrier cooling [34]. However, the red-detuned pump photon energies do not lead to hot carrier formation. The fast appearance of ΔOD in the presence of lower energy excitation is in line with our hypothesis that photo-induced holes introduce the transient response and no carrier cooling is involved in these scenarios [a schematic is presented in Fig. 3(e)].
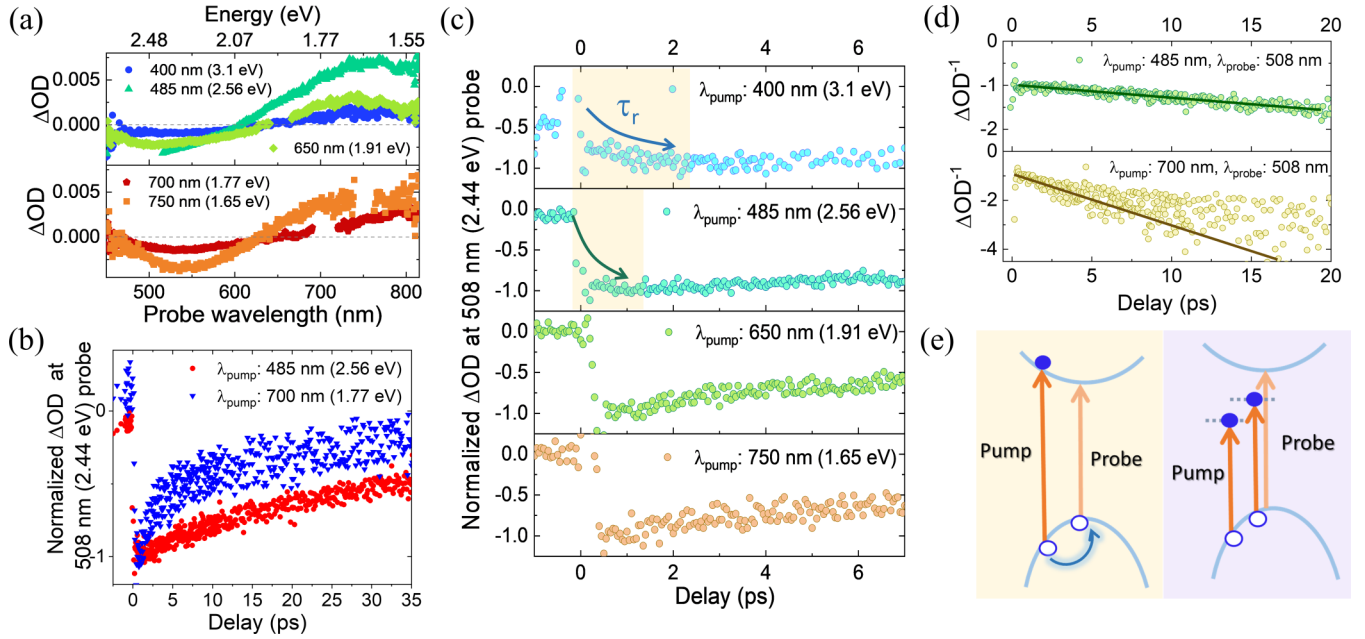
FIG. 3. (a) ΔOD spectrum at 1 ps probe delay following different pump excitations (indicated in the legend). (b) Normalized ΔOD decay dynamics at 508 nm (2.44 eV) probe wavelength upon 485 nm (2.56 eV) and 700 nm (1.77 eV) pump. (c) Normalized ΔOD dynamics at 508 nm probe wavelength up to 7 ps probe delay corresponding to 400 nm, 485 nm, 650 nm, and 750 nm pump excitation. (d) ΔOD^{-1} versus probe delay corresponding to 508 nm probe following 485 nm and 700 nm pump excitation. (e) A schematic model describing photoexcitation conditions for above-band and below-band pump excitations.

To highlight the carrier relaxation dynamics, normalized ΔOD at 508 nm ($\equiv 2.44$ eV), corresponding to 485 and 700 nm pump excitation, is plotted in Fig. 3(b). A fast decay process ($\sim$ few ps) is present for $\lambda_{pump} = 700$ nm in addition to the slower decay process; the former remains absent in the case of the 485 nm (see Fig. 4 of Ref. [14]). Further, it is verified that this additional fast decay component at 508 nm appears only when we tune the pump photon energy below this band gap E_{g2}.

As discussed previously, a linear variation of ΔOD^{-1} with probe delay indicates second-order recombination dynamics. Hence, we compare the temporal dynamics of ΔOD^{-1} at 508 nm (E_{g2}^{2D} band) for above- and below-band excitation. We identify deviation from linearity in the case of red-detuned pump excitation. Figure 3(d) compares this variation for 485 nm ($\equiv 2.56$ eV, above E_{g2} band gap) and 700 nm ($\equiv 1.77$ eV, below E_{g2} band gap) pump excitations. Notably, in the later case(s), ΔOD^{-1} does not follow exponential behavior, either. This confirms the absence of defect-assisted mono-molecular Shockley-Read-Hall (SRH) recombination. Aiming for further quantitative comprehension of the fast decay of the holes upon below-band-gap excitation and the indirect nature of electron-hole relaxation, we turn to identify the decay constants and the range of wavelengths where these components are prevalent. As the two timescales are different by one order, a simple bi-exponential decay model is employed to identify the two separate timescales,

$$\Delta OD(t) = A_f e^{-\frac{t}{\tau_f}} + A_s e^{-\frac{t}{\tau_s}}, \qquad (3)$$

where A_f and A_s denote two amplitude terms, and τ_f and τ_s indicate a fast and a slow decay component. The second-order,

slower relaxation is approximated with the exponential function here. Although we are unsure about the order and nature of the fast relaxation process, this assumption simply helps to identify the rough timescale associated. Repeated analyses for different probe wavelengths ranging from 470 nm through 575 nm allow us to map out the spectral dependence of the two decay components. In this range of wavelengths, the contribution from the ESA is insignificant, as confirmed in the global fitting. Figures 4(a) and 4(d) depict the decay constants in a broad range of probe wavelengths following 650 nm and 700 nm excitation, respectively. Wavelength-invariant decay constants are found to have following values: $\tau_f \sim 2$ ps and $\tau_s \sim 32$ ps. Interestingly, the fast timescale (~ 2 ps) exactly matches with the relaxation time of the excited state dynamics mediated by the midgap states, that is $\frac{1}{k_2' N_0'} \approx \frac{1}{0.44} \approx 2.3$ ps. Therefore, we attribute this timescale to the recombination of the pump-induced electrons in the mid-gap level with the valance band hole states. Interestingly, the slower decay constant nearly matches with the electron-hole relaxation time ($\sim \frac{1}{k_2 N_0} \approx 23 \pm 2$ ps), as found for above-E_{g2} band-gap photoexcitation (Table II). This slow decay (corresponding to $k_2 N_0 = -0.043 \pm 0.003$) is invariant in the state-filling reversion dynamics regardless of the pump photon energy, as long as there are photo-induced holes in the corresponding valance band. This observation confirms that this carrier relaxation pathway is predominantly indirect.

3. Relative contributions of defect-assisted fast recombination and indirect, slow electron-hole recombination

The relative pre-exponential amplitudes, $\eta_f = \frac{A_f}{A_f + A_s}$ and $\eta_s = \frac{A_s}{A_f + A_s}$, are presented as a function of the probe
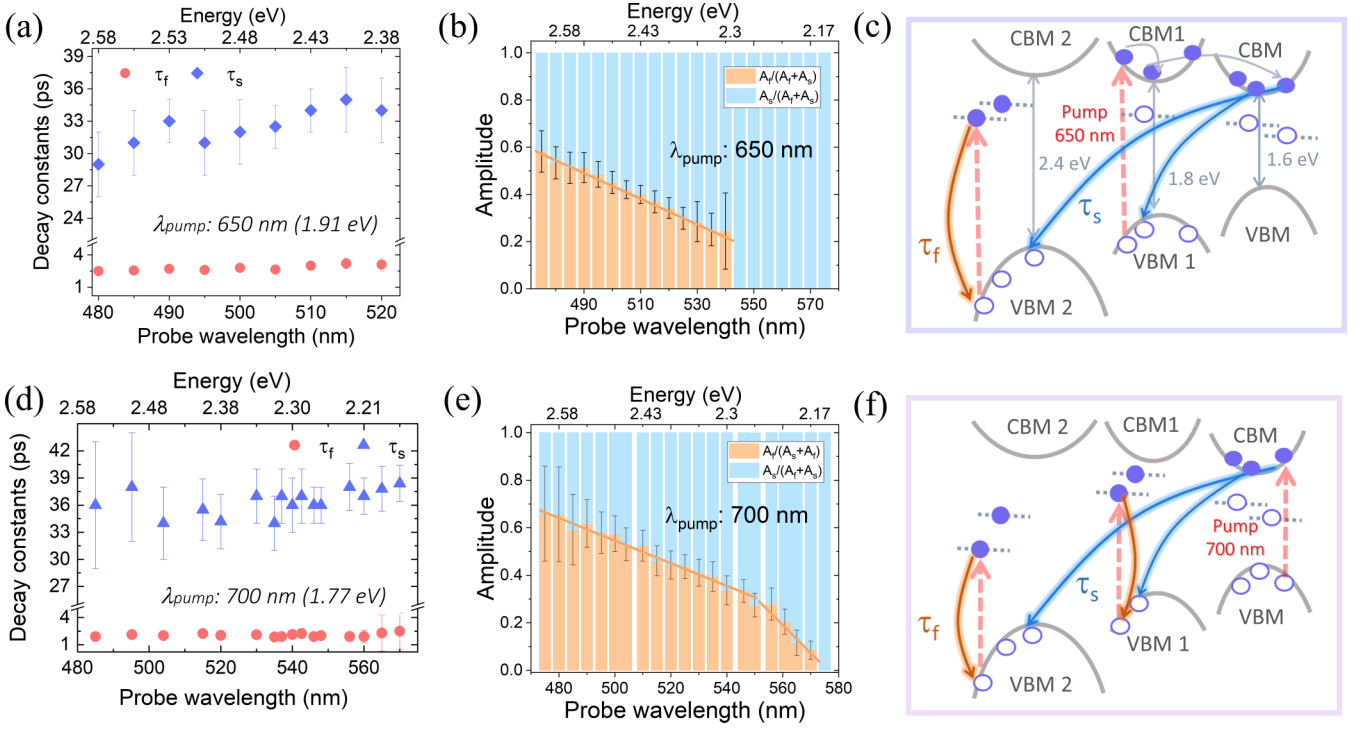
FIG. 4. (a) Fast and slow decay constants in the state-filling region as a function of the probe wavelength while the pump wavelength is 650 nm. (b) Normalized pre-exponential factors (/amplitude) corresponding to the two decay time scales as a function of the probe wavelength. (c) Schematic of the band diagram corresponding to 650 nm pump excitation. Pump-induced transitions are shown in dashed red arrows. Open and filled circles indicate holes and electrons, respectively. Fast and slow carrier relaxation pathways are identified as orange and cyan curved arrows. (d)–(f) Corresponding outputs for 700 nm pump excitation.

wavelength corresponding to $\lambda_{\text{pump}} = 650$ and 700 nm in Figs. 4(b) and 4(e). These weighted amplitudes display the relative contributions of the defect-assisted hole relaxation and indirect free electron-hole relaxation. Dynamics at different probe wavelengths reflect the carrier (hole) population dynamics in different valleys. Notably, under 650 nm (700 nm) photoexcitation, the contribution of the fast decay component related to the defect state to valance band recombination decreases with increasing probe wavelengths and is absent in the carrier dynamics above 540 nm (580 nm) probe (also see Sec. S5, Ref. [14]). We illustrate the overall scenario, including the defect-to-band and band-to-band recombination in the presence of 650 nm and 700 nm pump excitation through schematic band structures in Figs. 4(c) and 4(f).

The schematic band structure of GaTe shows the six different valleys in the conduction (CBM, CBM1, and CBM2) and valance bands (VBM, VBM1, VBM2) related to $E_g^{\text{2D}} = 1.6$ eV, $E_{g1}^{\text{2D}} = 1.8$ eV, and $E_{g2}^{\text{2D}} = 2.4$ eV band gaps that dominate optical absorption spectrum. The 650 nm ($\equiv 1.9$ eV) photoexcitation enables vertical electronic transition in CBM1 [right dashed arrow in Fig. 4(c)]. Although the electronic transition from VBM2 to CBM2 is energetically forbidden under 650 nm pump excitation, electrons from VBM2 may directly or indirectly fill up the midgap states [see left-most dashed arrow in Fig. 4(c)]. Such hole population leads to reduced probe absorption due to the state-filling effect. Note that the threshold of the fast decay component is around 2.3 eV, which nearly matches with E_{g2}^{2D}, confirming the defect-

related recombination is relevant for E_{g2}, i.e., in VBM2. The ~ 0.1 eV redshift of the threshold value from E_{g2} could be attributed to band-gap renormalization effect [35]. These holes in VBM2 recombine with the photoexcited electrons in the midgap levels or the free electrons in the conduction band minima (CBM and CBM1). As deduced numerically, these processes occur at ~2 ps and ~32 ps, respectively. In the case of 700 nm ($\equiv 1.77$ eV) pump excitation, photon energy is slightly redshifted with the band gap E_{g1}^{2D}. In contrast to the 650 nm excitation, sub-band-gap defect levels may be populated by the intense pump absorption [see dashed lines in Fig. 4(f)], particularly away from the band edge of VBM1. Therefore, we observed small contributions of fast decay (η_f) in the wavelength range 540 nm to 580 nm. The 700 nm pump enables the valance band to midgap state transition from the VBM2 as well. Hence, η_f values corresponding to the probe photon energy above 2.3 eV are similar to that of 650 nm pump excitation. The main difference between Figs. 4(b) and 4(e) is the nonzero η_f below 2.3 eV in the later plot. This arises due to VBM1 to midgap transitions enabled by the 700 nm (1.77 eV) pump excitation. The nonvanishing tail of the Tauc's plot at the lower energetic region (below the FBG), as depicted in Fig. 1(e) also supports the presence of such midgap states. As our observations indicate, the slower relaxation timescale is not affected by the variation of the pump photon energy. This suggests that the photoinduced carriers promoted to the conduction bands always recombine through slow, indirect processes.
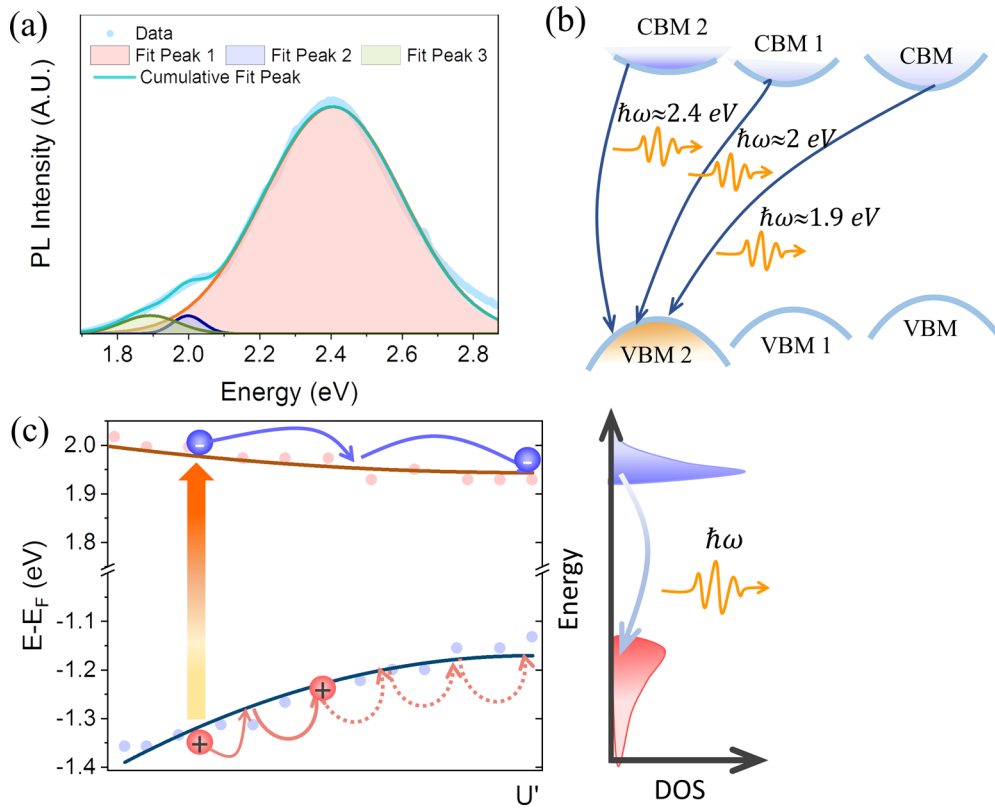
FIG. 5. (a) Steady-state photoluminescence (PL) spectrum of few-layered GaTe (with 405 nm laser excitation). The experimental data is fitted by three Gaussian functions. (b) Schematic diagram of the phonon-induced radiative decay mechanism. (c) Left panel: Energy-momentum distribution around U' point of Brillouin zone that corresponds to the band E_{g2}. Scatter plots represent the data extracted from Ref. [19] and the solid lines are the parabolic fits to the data. Right panel: Schematic energy versus density of states (DOS) corresponding to the band structure in the left panel. Hole temperature is higher at any time before equalization of carrier and lattice temperature that takes hundreds of ps to ns time. Hence, before complete carrier cooling, the carrier distribution in the valance band is broader than the electrons in the conduction band. Indirect, phonon-assisted radiative recombination in this band, therefore, leads to a broad PL spectrum.

4. Reason for indirect carrier relaxation

To see whether the carrier recombination process is radiative in nature, we perform steady-state photoluminescence (PL) of the few-layered GaTe flakes. Figure 5(a) presents the PL spectrum in the presence of 405 nm CW laser excitation. A broad PL is observed in the spectral range $\sim$ 1.8–2.8 eV. Therefore, it is quite plausible that the second-order recombination of the free carriers is radiative in nature. The obtained spectrum is fitted with three Gaussian peaks centered around 1.9 eV, 2 eV, and 2.4 eV. A broad, intense emission around 2.4 eV suggests radiative recombination of the carriers in the E_{g2}^{2D} band. The large broadening of the peak may originate from phonon-assisted hot carrier recombination. Precisely, the involvement of large momentum phonons enable radiative recombination of carriers in a broad spectral range [see Figs. 5(b) and 5(c)]. This again bolsters our conclusion of indirect carrier relaxation in the direct band. The other two peaks at 1.9 eV and 2 eV are offset by $\sim200-300$ meV with the direct bands E_g^{2D} and E_{g1}^{2D}. We attribute these peaks to phonon-assisted radiative recombination from CBM1$\rightarrow$ VBM2 and CBM $\rightarrow$ VBM2 [Fig. 5(b)]. Notably, the steady-state PL spectra is a time-integrated response. Time-resolved PL spectra and temperature-dependent steady-state PL spec-

tra would provide further information on the involvement of phonons in radiative recombination, which is beyond the scope of this paper.

At this point, it is important to address the reason for an indirect carrier relaxation in GaTe. As per the DFT calculations [19], the ratio of effective masses at the U' point is $\frac{m_e*}{m_h*} = 4.4$; hence, holes possess the dominant fraction of excess kinetic energy, $\Delta E_h = (\hbar\omega - E_{g2}^{2D})(\frac{m_e*}{m_e*+m_h*}) = 0.82 \times (\hbar\omega - E_{g2}^{2D})$. Light holes possessing higher kinetic energy than the heavy electrons need to emit more phonons than the electrons do [see Fig. 5(c)]. Due to this mismatch of the electron and hole effective masses, the quasimomentum of the two entities differ at any instant in the temporal window from photoexcitation to complete carrier cooling, leading to a negligible probability of direct recombination. Therefore, the favorable path for carrier relaxation is indirect recombination, which involves the absorption or emission of phonons.

5. Role of defect states in carrier dynamics

As highlighted in the previous section, carrier relaxation dynamics in the few-layered GaTe are mostly dictated by indirect electron-hole recombination. However, defect states often have some contribution in the free carrier dynamics of
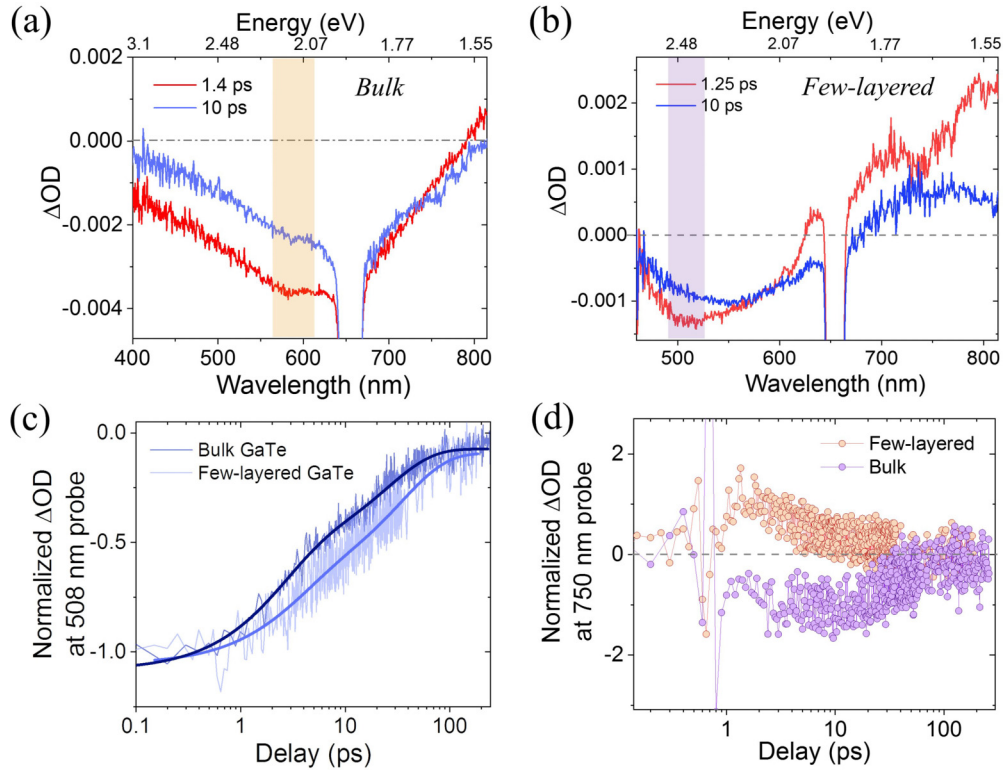
FIG. 6. (a) ΔOD spectrum at 1.4 ps and 10 ps following 650 nm pump excitation in bulk GaTe. The yellow bar indicates the region where $-\Delta OD$ has the highest amplitude. (b) ΔOD spectra at 1.25 ps and 10 ps following 650 nm pump excitation in few-layered GaTe. The purple bar indicates the maximum $-\Delta OD$ amplitude. Normalized ΔOD dynamics with respect to the maximum $|\Delta OD|$ at (c) 508 nm and (d) 750 nm probe following 650 nm excitation of the bulk and few-layered GaTe.

different valleys. To highlight the effect of defect density, differential absorption in bulk and few-layered GaTe is compared. Owing to the vacancy of atoms in the material surface, midgap states are created [13]. The surface-to-volume ratio in a 25-nm-thick flake (few-layered) is higher than that of a 150-nm-thick flake (bulk). Hence, the thick GaTe possesses much less defect density as many defects are observed at the surfaces. Figures 6(a) and 6(b) display the ΔOD spectra of bulk and few-layered GaTe at two selected probe delays. Notably, the maximum of $-\Delta OD$ lies around 580 nm (≈ 2.1 eV) and 510 nm (≈ 2.4 eV) in the bulk and few-layered samples that are consistent with the higher energetic band gaps (E_{g1}^{bulk} and E_{g2}^{2D}) as observed in Fig. 2(c) of Ref. [14] and Fig. 1(e). Figure 6(c) compares the normalized ΔOD dynamics at 508 nm of the two samples. The relaxation process in the few-layered sample is slightly slower than the bulk one, possibly due to the size-confinement effect in the former. If the defect state directly affected the carrier relaxation, one would expect faster carrier relaxation in the few-layered GaTe. As displayed by Fig. 6(a), no ESA band is present in the visible wavelengths. It is quite intuitive and expected, considering the lower defect density in bulk GaTe. On a similar note, this observation strengthens our attribution of the midgap defect states to be involved as the intermediate levels in ESA. Furthermore, a comparison of normalized ΔOD dynamics at 750 nm in Fig. 6(d) portrays the difference in bulk and few-layered MMCs: bulk material displays state-filling dynamics, whereas few-layered GaTe exhibits ESA dynamics.

III. DISCUSSION

This work explores carrier dynamics following ultrafast optical excitation in a layered metal monochalcogenide-gallium telluride. This multivalley semiconductor exhibits at least three direct band gaps in the optical frequencies. However, interestingly, photoexcited carriers relax via indirect radiative processes. The dominant timescale for the indirect carrier relaxation is ~30 ps. In other atomically thin materials (like TMDCs), optical excitation decays within sub-ps to few ps timescales due to various defect-induced carrier capture, exciton recombination, or exciton-exciton annihilation. Unlike TMDCs, relaxation dynamics in GaTe are slower, owing to the absence of strong excitonic effects, higher-order carrier relaxation (like-Auger scattering), or fast carrier capture in the defects that typically take place in sub-ps to a few ps timescale [36–38]. The slow carrier relaxation in this direct band material that possesses high absorption oscillator strength is highly beneficial for efficient light-to-electricity conversion.

[1] F. H. L. Koppens, T. Mueller, P. Avouris, A. C. Ferrari, M. S. Vitiello, and M. Polini, Photodetectors based on graphene, other two-dimensional materials and hybrid systems, Nat. Nanotechnol. **9**, 780 (2014).

[2] F. Liu, H. Shimotani, H. Shang, T. Kanagasekaran, V. Zólyomi, N. Drummond, V. I. Fal'ko, and K. Tanigaki, High-sensitivity photodetectors based on multilayer gate flakes, ACS Nano **8**, 752 (2014).

[3] J. Kang, S. A. Wells, V. K. Sangwan, D. Lam, X. Liu, J. Luxa, Z. Sofer, and M. C. Hersam, Solution-based processing of opto-electronically active indium selenide, Adv. Mater. **30**, 1802990 (2018).

[4] T. Singha, M. Karmakar, P. Kumbhakar, C. S. Tiwary, and P. K. Datta, Atomically thin gallium telluride nanosheets: A new 2D material for efficient broadband nonlinear optical devices, Appl. Phys. Lett. **120**, 021101 (2022).

[5] Z. Wang, K. Xu, Y. Li, X. Zhan, M. Safdar, Q. Wang, F. Wang, and J. He, Role of Ga vacancy on a multilayer gate phototransistor, ACS Nano **8**, 4859 (2014).

[6] J. Kang, V. K. Sangwan, H.-S. Lee, X. Liu, and M. C. Hersam, Solution-processed layered gallium telluride thin-film photodetectors, ACS Photonics **5**, 3996 (2018).

[7] M. Huang, M. Wang, C. Chen, Z. Ma, X. Li, J. Han, and Y. Wu, Broadband black-phosphorus photodetectors with high responsivity, Adv. Mater. **28**, 3481 (2016).

[8] W. Zhang, J.-K. Huang, C.-H. Chen, Y.-H. Chang, Y.-J. Cheng, and L.-J. Li, High-gain phototransistors based on a CVD MoS$_2$ monolayer, Adv. Mater. **25**, 3456 (2013).

[9] O. Lopez-Sanchez, D. Lembke, M. Kayci, A. Radenovic, and A. Kis, Ultrasensitive photodetectors based on monolayer MoS$_2$, Nat. Nanotechnol. **8**, 497 (2013).

[10] S. R. Tamalampudi, Y.-Y. Lu, R. K. U., R. Sankar, C.-D. Liao, K. M. B., C.-H. Cheng, F. C. Chou, and Y.-T. Chen, High performance and bendable few-layered InSe photodetectors with broad spectral response, Nano Lett. **14**, 2800 (2014).

[11] T. J. Octon, V. K. Nagareddy, S. Russo, M. F. Craciun, and C. D. Wright, Fast high-responsivity few-layer MoTe$_2$ photodetectors, Adv. Opt. Mater. **4**, 1750 (2016).

[12] C. Jung, S. M. Kim, H. Moon, G. Han, J. Kwon, Y. K. Hong, I. Omkaram, Y. Yoon, S. Kim, and J. Park, Highly crystalline CVD-grown multilayer MoSe$_2$ thin film transistor for fast photodetector, Sci. Rep. **5**, 15313 (2015).

[13] S. Siddique, C. C. Gowda, R. Tromer, S. Demiss, A. R. S. Gautam, O. E. Femi, P. Kumbhakar, D. S. Galvao, A. Chandra, and C. S. Tiwary, Scalable synthesis of atomically thin gallium telluride nanosheets for supercapacitor applications, ACS Appl. Nano Mater. **4**, 4829 (2021).

[14] See Supplemental Material at http://link.aps.org/supplemental/10.1103/PhysRevB.107.075429 for additional discussion on sample characterization, experimental techniques, and data analysis.

[15] M. M. Glazov and A. Chernikov, Breakdown of the static approximation for free carrier screening of excitons in monolayer semiconductors, Phys. Status Solidi (b) **255**, 1800216 (2018).

[16] J. Hong, Z. Hu, M. Probert, K. Li, D. Lv, X. Yang, L. Gu, N. Mao, Q. Feng, L. Xie, J. Zhang, D. Wu, Z. Zhang, C. Jin, W. Ji, X. Zhang, J. Yuan, and Z. Zhang, Exploring atomic defects in molybdenum disulphide monolayers, Nat. Commun. **6**, 6293 (2015).

[17] A. Yamamoto, A. Syouji, T. Goto, E. Kulatov, K. Ohno, Y. Kawazoe, K. Uchida, and N. Miura, Excitons and band structure of highly anisotropic gate single crystals, Phys. Rev. B **64**, 035210 (2001).

[18] A. Zubiaga, J. A. Garcıa, F. Plazaola, V. Muñoz-Sanjosé, and M. C. Martınez-Tomás, Recombination processes in unintentionally doped gate single crystals, J. Appl. Phys. **92**, 7330 (2002).

[19] S. Huang, Y. Tatsumi, X. Ling, H. Guo, Z. Wang, G. Watson, A. A. Puretzky, D. B. Geohegan, J. Kong, J. Li, T. Yang, R. Saito, and M. S. Dresselhaus, In-plane optical anisotropy of layered gallium telluride, ACS Nano **10**, 8964 (2016).

[20] J. F. Sánchez-Royo, A. Segura, and V. Muñoz, Anisotropy of the refractive index and absorption coefficient in the layer plane of gallium telluride single crystals, Phys. Status Solidi (a) **151**, 257 (1995).

[21] J. J. Fonseca, S. Tongay, M. Topsakal, A. R. Chew, A. J. Lin, C. Ko, A. V. Luce, A. Salleo, J. Wu, and O. D. Dubon, Bandgap restructuring of the layered semiconductor gallium telluride in air, Adv. Mater. **28**, 6465 (2016).

[22] A. J. Niilisk and J. J. Kirs, Photoconductivity of gas, GaSe, and gate single crystals under high hydrostatic pressure, Phys. Status Solidi (b) **31**, K91 (1969).

[23] F. Urbach, The long-wavelength edge of photographic sensitivity and of the electronic absorption of solids, Phys. Rev. **92**, 1324 (1953).

[24] M. Karmakar, S. Bhattacharya, S. Mukherjee, B. Ghosh, R. K. Chowdhury, A. Agarwal, S. K. Ray, D. Chanda, and P. K. Datta, Observation of dynamic screening in the excited exciton states in multilayered MoS$_2$, Phys. Rev. B **103**, 075437 (2021).

[25] M. Karmakar, S. Mukherjee, S. K. Ray, and P. K. Datta, Electron-hole plasma formation dynamics observed through exciton-plasma interactions in transition metal dichalcogenides, Phys. Rev. B **104**, 075446 (2021).

[26] S. Bhattacharya, A. Ghorai, S. Raval, M. Karmakar, A. Midya, S. K. Ray, and P. K. Datta, A comprehensive dual beam approach for broadband control of ultrafast optical nonlinearity in reduced graphene oxide, Carbon **134**, 80 (2018).

[27] K. Basu, H. Zhang, H. Zhao, S. Bhattacharya, F. Navarro-Pardo, P. K. Datta, L. Jin, S. Sun, F. Vetrone, and F. Rosei, Highly stable photoelectrochemical cells for hydrogen production using a SnO$_2$–TiO$_2$/quantum dot heterostructured photoanode, Nanoscale **10**, 15273 (2018).

[28] S. W. Koch, M. Kira, G. Khitrova, and H. M. Gibbs, Semiconductor excitons in new light, Nat. Mater. **5**, 523 (2006).

[29] G. Xing, B. Wu, X. Wu, M. Li, B. Du, Q. Wei, J. Guo, E. K. L. Yeow, T. C. Sum, and W. Huang, Transcending the slow bimolecular recombination in lead-halide perovskites for electroluminescence, Nat. Commun. **8**, 14558 (2017).

[30] L. Wang, Z. Wang, H.-Y. Wang, G. Grinblat, Y.-L. Huang, D. Wang, X.-H. Ye, X.-B. Li, Q. Bao, A.-S. Wee, S. A. Maier, Q.-D. Chen, M.-L. Zhong, C.-W. Qiu, and H.-B. Sun, Slow cooling and efficient extraction of c-exciton hot carriers in MoS$_2$ monolayer, Nat. Commun. **8**, 13906 (2017).

[31] M. Lorenc, M. Ziolek, R. Naskrecki, J. Karolczak, J. Kubicki, and A. Maciejewski, Artifacts in femtosecond transient absorption spectroscopy, Appl. Phys. B **74**, 19 (2002).

[32] B. Baudisch, Time resolved broadband spectroscopy from UV to NIR, Ph.D. thesis, Munich, Germany, 2018.

[33] M. Karmakar and P. K. Datta, Comment on "Ultrafast insights into high energy (C and D) excitons in few layer WS$_2$," J. Phys. Chem. Lett. **13**, 5953 (2022).

[34] M. B. Price, J. Butkus, T. C. Jellicoe, A. Sadhanala, A. Briane, J. E. Halpert, K. Broch, J. M. Hodgkiss, R. H. Friend, and F. Deschler, Hot-carrier cooling and photoinduced refractive index changes in organic–inorganic lead halide perovskites, Nat. Commun. **6**, 8420 (2015).

[35] E. A. A. Pogna, M. Marsili, D. De Fazio, S. Dal Conte, C. Manzoni, D. Sangalli, D. Yoon, A. Lombardo, A. C. Ferrari, A. Marini, G. Cerullo, and D. Prezzi, Photo-induced bandgap renormalization governs the ultrafast response of single-layer MoS$_2$, ACS Nano **10**, 1182 (2016).

[36] H. Shi, R. Yan, S. Bertolazzi, J. Brivio, B. Gao, A. Kis, D. Jena, H. G. Xing, and L. Huang, Exciton dynamics in suspended monolayer and few-layer MoS$_2$ 2D crystals, ACS Nano **7**, 1072 (2013).

[37] S. H. Aleithan, M. Y. Livshits, S. Khadka, J. J. Rack, M. E. Kordesch, and E. Stinaff, Broadband femtosecond transient absorption spectroscopy for a CVD Mos$_2$ monolayer, Phys. Rev. B **94**, 035445 (2016).

[38] C. Ruppert, A. Chernikov, H. M. Hill, A. F. Rigosi, and T. F. Heinz, The role of electronic and phononic excitation in the optical response of monolayer WS$_2$ after ultrafast excitation, Nano Lett. **17**, 644 (2017).